machines

MDPI

Article

Biomimetic Origami: Planar Single-Vertex Multi-Crease Mechanism Design and Optimization

Yihang Wang [1], Yongsheng Zhao [1,2], Bo Han [1,2,*], Jinming Dong [1], Meng Han [3] and Jiantao Yao [1,2]

[1] School of Mechanical Engineering, Yanshan University, Qinhuangdao 066004, China; yh_wang@stumail.ysu.edu.cn (Y.W.); yszhao@ysu.edu.cn (Y.Z.); dongjinming@stumail.ysu.edu.cn (J.D.); jtyao@ysu.edu.cn (J.Y.)
[2] Hebei Provincial Key Laboratory of Parallel Robot and Mechatronic System, Yanshan University, Qinhuangdao 066004, China
[3] College of Information Science and Engineering, Northeastern University, Shenyang 110819, China; hanmeng@neuq.edu.cn
* Correspondence: bohan@ysu.edu.cn

Abstract: Space exploration and satellite communication demand lightweight, large-scale, and highly deployable structures. Inspired by the folding mechanism of frilled lizards and origami mechanisms, this study explores a deployable structure based on the single-vertex multi-crease origami (SVMCO) concept. The design focuses on crease distribution optimization to enhance deployment efficiency. A mathematical model analyzes the relationship between sector angles of three types of facets and structural performances, providing guidelines for achieving optimal deployment. Drawing from the rib patterns of frilled lizards, a rib support system for thick-panel mechanisms was designed and verified through a physical prototype. The structure achieves smooth-surface deployment with fewer supports, offering a lightweight and efficient solution for deployable systems.

Keywords: biomimetic design; origami mechanisms; single-vertex multi-crease origami; deployable structures; origami crease optimization

check for updates

Academic Editor: Huosheng Hu

Received: 21 January 2025
Revised: 4 March 2025
Accepted: 10 March 2025
Published: 17 March 2025

Citation: Wang, Y.; Zhao, Y.; Han, B.; Dong, J.; Han, M.; Yao, J. Biomimetic Origami: Planar Single-Vertex Multi-Crease Mechanism Design and Optimization. *Machines* **2025**, *13*, 240. https://doi.org/10.3390/machines13030240

Copyright: © 2025 by the authors. Licensee MDPI, Basel, Switzerland. This article is an open access article distributed under the terms and conditions of the Creative Commons Attribution (CC BY) license (https://creativecommons.org/licenses/by/4.0/).

1. Introduction

Deployable structures have seen growing applications in aerospace, robotics, and related engineering fields, with their lightweight and efficient designs significantly improving space utilization [1–3]. In aerospace, Kim's team [4] developed scissor-like foldable trusses for flat storage, while Han's group [5–7] enhanced satellite antenna systems through hexagonal prism mechanisms and rectangular pyramid units, demonstrating reliable kinematic control in dynamic environments.

Origami-inspired approaches have opened new design possibilities, as shown in Figure 1. Carefully engineered crease patterns enable flat sheets to fold into compact forms and deploy into complex 3D shapes [8]. Fundamental folding mechanisms were established through studies on multi-vertex configurations [9–11], while subsequent engineering applications explored programmable curved surfaces [12,13]. Building on these principles, Vlachaki et al. [9] integrated origami with vaulted structures, and Tang's team [10] created rotating space-deployable devices using spiral crease patterns. Communication technology applications include Zhang's reconfigurable antennas [11], supported by Fonseca's mechanical framework [12]. These innovations extend to modular units [14–17] and multi-scale control systems coordinating microscopic folding with macroscopic deployment [16–18].

The design methods of origami mechanisms come from various sources [19]. They include mathematical derivations [20,21] and inspirations from nature, which artists and

scientists have observed and summarized. Many biological structures in nature offer valuable insights for origami design [22–24]. For example, the wings of beetles provide unique inspiration [24]. Their fan-shaped wings, with radially arranged venation patterns, show a natural single-vertex multi-crease origami (SVMCO) design (Figure 1d). In this structure, several folds converge at a central point to enable compact folding and rapid deployment. By mimicking these efficient folding and unfolding mechanisms from nature, origami designs can achieve compact storage and, when unfolded, a larger functional form.

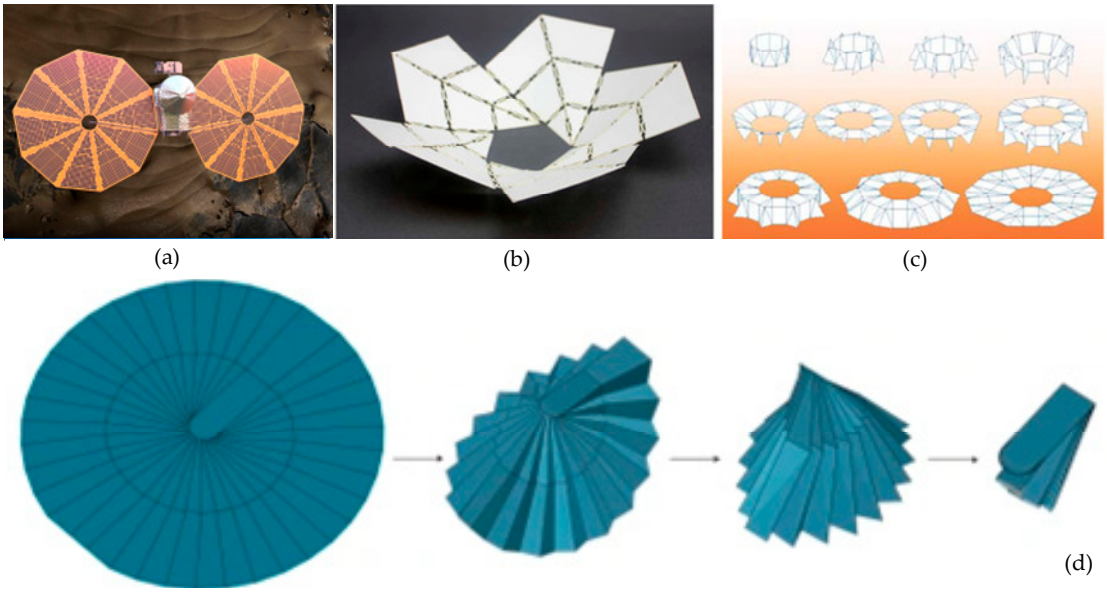

Figure 1. Applications of deployable origami structures in aerospace: (**a**) NASA's Lucy mission, (**b**) deployable antenna [25], (**c**) foldable telescopic lens [26], and (**d**) origami inspired by insect wings [24].

This form of origami creates multiple creases emanating from a single point, allowing for the construction of highly intricate and complex geometric forms [27,28]. In contrast to traditional origami, which distributes creases across several vertices, SVMCO focuses on concentrating creases at a single vertex [29]. This approach offers new possibilities for creating more compact and efficient designs, especially in applications that require precise control over shape transformation. SVMCO is particularly useful in deployable structures and mechanical metamaterials [30–33], where manipulating multiple creases from a single vertex enhances control over movement and transformation.

Single-vertex multi-crease origami (SVMCO) structures use circular folding patterns that work like mechanical linkages. Researchers have found that their folding behaviours depend heavily on three key factors: the angles between creases, the length of folds, and how thick the panels are [34–36]. For example, studies show that changing the central angle of folds—like switching from 60° to 90° designs—can drastically affect how these structures move and hold weight [37,38]. To ensure smooth deployment, engineers carefully plan the crease patterns. They create alternate mountain and valley folds in radiating patterns to reduce stress and use computer models to balance movement and material strain [39–41]. Recent improvements focus on making these structures lighter yet strong. One method thins out non-essential panels without losing stiffness [42,43], while another uses algorithms to design folds that absorb energy better [44].

Although progress has been made in SVMCO-based designs, research is still ongoing, with several challenges and gaps remaining. Most existing studies focus on arrays with a small number of units, and there is limited research on how the number of units affects overall folding and unfolding characteristics. Furthermore, many studies are based on

idealized models without considering the real-world challenges of thickened panels, which are critical for engineering applications. Addressing these issues will help explore the unique properties of SVMCO and provide references for designing deployable structures, especially those that require precise shape control.

To address these issues in current origami models, this study develops a new mathematical model by analysing the umbrella-like structure of the frilled lizard's frills. The model incorporates panel thickness to better simulate structural behaviour in real-life applications. Specifically, it will analyse how the number of units affects foldability and deployment efficiency and explore how adjusting the panel angle ratios and thickness can optimize the SVMCO design to improve foldability. This study aimed to deepen the understanding of the SVMCO structure's performance in practical engineering scenarios by imitating its efficient single-vertex multi-crease folding mechanism, providing theoretical support for future applications of deployable structures based on origami principles.

The structure of this paper is as follows: Section 2 will discuss the theoretical analysis and model development, introducing the inspiration from the frilled lizard's biomimetic design and analysing ways to optimize the SVMCO structure by combining panel thickness and angle ratios. Section 3 will outline experimental methods and prototype design. Section 4 will present experimental results and provide a detailed discussion. Finally, Section 5 will summarize the research findings and suggest future research directions.

2. Single-Vertex Multi-Crease Origami Pattern Design

2.1. Identification of Origami Unit Types

Research on single-vertex multi-crease origami (SVMCO) patterns focuses on the distribution of mountain and valley folds, as they directly affect the final folded shape. In traditional biomimicry of single-vertex multi-crease structures, researchers often simplify the creases in biological structures into Z-shaped folds. This simplification arises for two reasons. First, the biological structure under study often resembles a thin film with negligible thickness. Second, researchers tend to focus on the behaviour of these structures during transitions between flat planes, treating them as thickened panels regardless of folding or unfolding.

In the simple Z-shaped folding, mountain and valley folds alternate, and the folded state appears as shown in Figure 2. However, applying this folding method directly to curved surfaces introduces vertical offsets Δh at the crease vertices, resulting in upward spiral displacements ΔS at the connections, as shown in Figure 3. These displacements prevent the origami pattern from forming a closed loop at crease rotation angles between 0° and 180°. The total offset equals the sum of the individual offsets Δs_i from each origami unit. To achieve a closed-loop structure, axial displacements must be incorporated into the design of Z-shaped folds. This adjustment adds complexity to the structure.

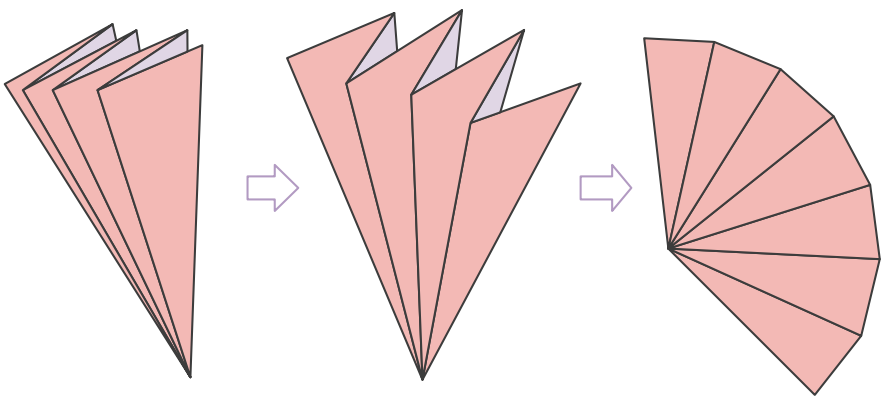

Figure 2. Deployment sequence of the Z-shaped crease.

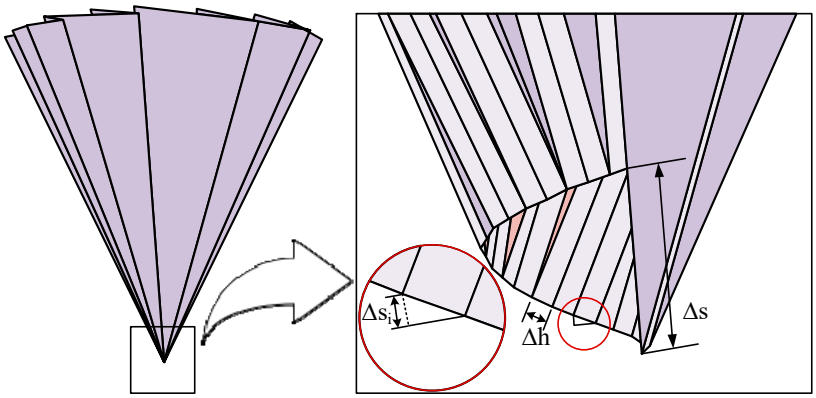

Figure 3. Upward displacement Δs during Z-folding prevents crease junction overlapping.

In nature, structures with significant thickness can also fold and unfold curved surfaces effectively. The frill of the frilled lizard serves as a prime example. Unlike the linear venation in insect wings, the frill's surface features wrinkles with three ridges forming on each lobe of the fringe. Research from [45] indicated that these ridges arise from elastic instabilities during the development of the branchial ectoderm, a result of natural selection.

When the frilled lizard folds or unfolds its thick frill, the distribution of mountain and valley folds becomes more complex than a simple Z-shaped folding, which shown in Figure 4. The structure adds more folds, forming a mirrored arrangement of two Z-shaped folds, termed here as the Ω-shaped folding unit.

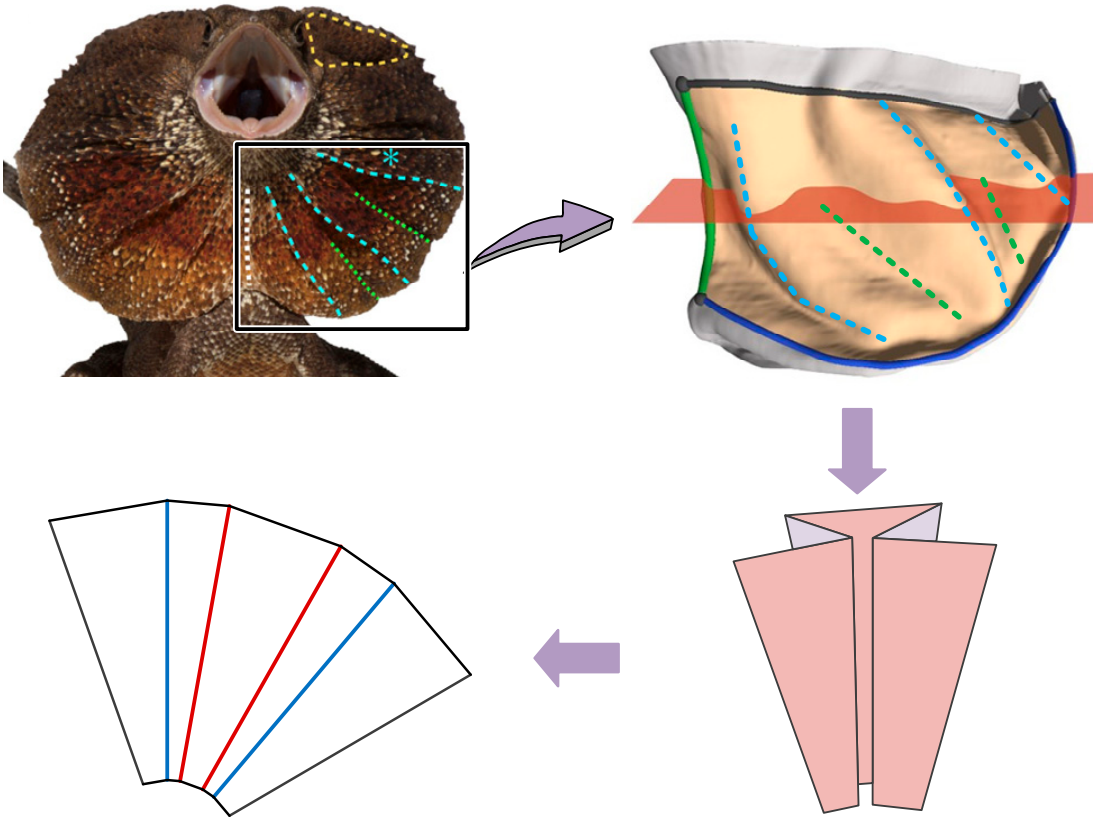

Figure 4. Biomimetic design of origami creases inspired by the wrinkled distribution [45] on the frill of the frilled lizard (red lines: mountain creases, blue lines: valley creases).

As shown in Figure 5, this closed deployable structure consists of three types of facets, named facet1, facet-2, and facet-3, arranged according to their increasing facet angle. An Ω-shaped folding unit comprises two facet-1s, one facet-2, and one facet-3.

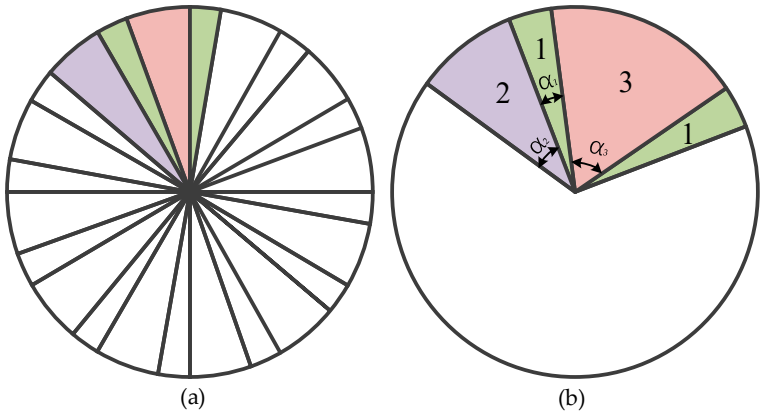

Figure 5. Unit division of origami pattern; (**a**) origami pattern divided into 6 Ω-shaped folding units and 24 facets, (**b**) Ω-shaped crease divided into four smaller sub-facets α_1.

In the Ω-shaped folding unit, the distribution of creases in the sub-unit origami pattern changes from "mountain-valley-mountain-valley" to "mountain-mountain-valley-valley". When the first Z-shaped unit of the Ω-shaped folding unit generates an upward offset of length Δs_i, the second Z-shaped unit, which is mirror-symmetrical to the first, generates a downward axial offset of length Δs_{i+1}. After the offsets of the two Z-shaped sub-units cancel each other out, the total offset of the Ω-shaped fold is zero, meeting the requirement for sub-unit connection into a ring.

2.2. Determination of the Number of Origami Units

When designing a complete crease pattern starting with Ω-shaped units, several factors require consideration for mathematical analysis and optimization. The number of Ω-shaped units is a critical aspect. Evaluating this number involves assessing the folding ratio, manufacturing complexity, and structural reliability. The choice of unit count directly influences deployment performance and must take priority in the design as shown in Figure 6.

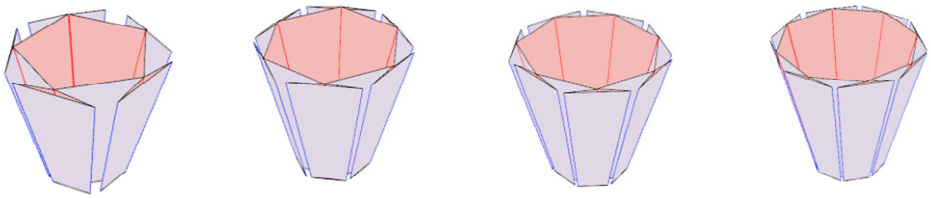

Figure 6. Effect of different unit numbers on the folded shape when the sector angle ratio is constant.

To simplify analysis, assume each unit transforms from a plane into a truncated polyhedron during folding. At least three Ω-shaped units are needed to create a continuous closed-loop structure. In the engineering application of space antennas, besides forming a closed-loop structure, the folding ratio is also an important reference factor. Folding ratio is a key metric for measuring the antenna's foldability and portability. It is defined as the ratio of the antenna's radial dimensions in the folded state to those in the deployed state. A lower folding ratio means the antenna takes up less space when folded, making transportation easier and reducing the cost. Calculations show that the folding ratio increases with the number of units and approaches 0.25 as the unit count approaches infinity.

The design must also consider the impact of the smallest facet angle on manufacturing precision. Extremely small angles increase production and assembly challenges, raising costs and reducing reliability. Designs should avoid excessively small facet angles. Based on the relationships between unit count, folding ratio, and minimum facet angle, results

indicate that the unit count should remain between 3 and 10. Fewer than 3 units are insufficient to form a continuous closed-loop structure, while more than 10 units greatly increase manufacturing and assembly challenges without significant gains in folding ratio performance.

Additionally, the number of facets significantly affects complexity and reliability. Adding more facets introduces additional hinges and panels, increasing structural complexity and internal gaps while reducing reliability. Assuming each crease connects through two hinges, a relationship between unit count and hinge count emerges.

Analysis of these factors leads to several conclusions. The foldability ratio decreases with increasing unit count, with the rate of change slowing around seven units. Similarly, changes in the smallest facet angle also slow at this point. Furthermore, component count increases linearly with unit count. Table 1 illustrates these trends for different unit numbers.

Table 1. Parameters for varying numbers of units.

Number of Units	Folding Ratio	Minimum Facet Angle	Number of Facets
3	0.5047	20	24
4	0.4382	15	32
5	0.4037	12	40
6	0.3836	10	48
7	0.3709	8.571429	56
8	0.3625	7.5	64
9	0.3566	6.666667	72
10	0.3523	6	80

The final determination of the unit number is affected by several factors. Each of these factors has a varying level of impact. To address this complexity, the Analytic Hierarchy Process (AHP) is introduced as a comprehensive evaluation system. This system will assess the influence weight of each factor on the final number of units. In the hierarchical analysis, we constructed a two-by-two comparison matrix for each of the three indicators and determined the relative weights of each item according to the importance of expert scores or design requirements. Specifically, a judgment matrix (a table comparing factors in pairs) is constructed using the 1–9 scale (e.g., 1 = equal importance, 9 = extreme dominance of one factor over another). The importance of each factor is determined according to the design requirements set by the launch vehicle's payload constraints. Pairwise comparisons are used to create the evaluation matrix A, as follows:

$$A = \begin{bmatrix} 1 & 4 & 4 \\ \frac{1}{4} & 1 & \frac{1}{2} \\ \frac{1}{4} & 2 & 1 \end{bmatrix} \tag{1}$$

where $a_{i,j}$ quantifies the relative importance of criterion i over j.

Then, normalized weights matrix W are calculated through eigenvector analysis:

$$W = [w_1, w_2, \ldots, w_n]^T \tag{2}$$

where $w_i = \frac{1}{n} \sum_{j=1}^{n} \frac{a_{i,j}}{\sum_{k=1}^{n} a_{k,j}}$, while $a_{i,j}$ quantifies the relative importance of criterion i over j.

Subsequently, the normalised weights of the criteria were derived by solving the eigenvector associated with the maximum eigenvalue λ_{max} of the pairwise comparison

matrix A. To validate the logical consistency of the expert judgments, the consistency ratio (CR) was calculated as:

$$CR = \frac{\lambda_{max} - n}{(n-1)RI} \tag{3}$$

where $\lambda_{\max=}\frac{1}{n}\sum_{i=1}^{n}\frac{(AW)_i}{w_i}$, n = 3 (number of criteria), and RI = 0.58 (the random consistency index for a 3 × 3 matrix, obtained from standardized AHP reference tables).

The consistency ratio in this study is about 0.051, which is much lower than the common threshold of 0.1, indicating good internal consistency in weight assignment. As shown in Table 2, foldability receives the highest normalised weight (0.6551) in the overall trade-off, indicating that it is crucial to the optimization of the folding unit. Meanwhile, the number of facets and the maximum sector angle are 0.2114 and 0.1335, respectively, reflecting the need to take into account the degree of simplification of the structure and the machining feasibility while satisfying the need for folding. This quantification process helps determine the importance of each design goal and provides a clear way to improve the folding unit. The AHP method ensures a fair and structured evaluation, allowing us to balance different factors and choose the best design based on the data.

Table 2. The influence weight of each factor on the final number of units.

Influence Factor	Contribution to Folding Ratio	Contribution to Minimum Sector Angle	Contribution to Number of Facets	Normalized Weights
1. Folding ratio	1.00	4.00	4.00	0.655
2. Minimum sector Angle	0.25	1.00	0.50	0.133
3. Number of facets	0.25	2.00	1.00	0.211

To summarize the influence of each factor, the weighted scores were calculated and compiled into Table 3. It combines information from Tables 1 and 2 to calculate the final scores. Table 1 lists the influence factors, such as folding ratio, minimum facet angle, and number of facets, while Table 2 provides their importance weights. In the current evaluation system, these influence factors are adjusted to a 1–10 scale for easy comparison. For parameters where smaller values indicate better performance (such as folding ratio and number of facets), higher scores are assigned to lower values. Conversely, for the minimum facet angle, where a larger value is preferable, the scoring is reversed. This ensures that higher scores always indicate better performance.

Table 3. The score for varying numbers of units.

Number of Units	Folding Ratio	Score
3	0.5047	13.0642
4	0.4382	13.5537
5	0.4037	13.6501
6	0.3836	13.8317
7	0.3709	13.7613
8	0.3625	13.7465
9	0.3566	13.5351
10	0.3523	13.7316

After obtaining the normalized score for each factor, the final weighted score can be calculated by summing the weighted contributions based on the weights listed in Table 2. Table 3 presents the relationship between the number of units, folding ratio, and final

weighted score. The folding ratio decreases as the number of units increases, but the weighted score varies due to the trade-offs between different factors. The highest score is observed at six units, suggesting an optimal balance based on the current evaluation system.

2.3. Dimensional Analysis and Optimization of Single-Vertex Multi-Crease Origami Patterns

The previous discussion covered the impact of unit quantity on SVMCO patterns. In addition, the angle proportions between facets1, facets2, and facets3 are also crucial factors to consider when designing crease patterns. By adjusting the angle proportions, the structure can be modified to find the optimal folding ratio. This process not only affects the overall shape of the origami pattern but also directly influences its functional performance and practical application.

By observing the projected shapes with the maximum projection area, it can be found that adjusting the angle proportions between facets1, facets2, and facets3 results in three different states, as shown in Figure 7. These three states not only exhibit noticeable visual differences but also demonstrate unique characteristics in practical applications. The calculation process for the folding ratio varies for each state, and these differences need to be considered and optimized in the specific design to ensure an optimal performance of the origami structure in different application scenarios. The following sections will discuss the three folding methods separately.

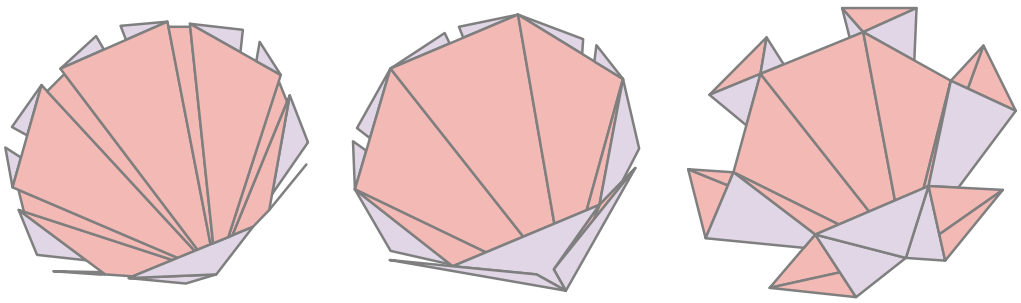

(a) (b) (c)

Figure 7. Three folding states based on different relationships between and α_1; (**a**) folded state when $\alpha_3 > 2\alpha_1$, (**b**) folded state when $\alpha_3 = 2\alpha_1$, and (**c**) folded state when $\alpha_3 < 2\alpha_1$.

Let α_1 denote the sector angle corresponding to facets1, α_2 the sector angle corresponding to facets2, and α_3 the sector angle corresponding to facets3. Since there are 6 Ω origami units ($n = 6$), each unit occupies an angle of 60°. Therefore,

$$2\alpha_1 + \alpha_2 + \alpha_3 = 60^\circ \tag{4}$$

When $\alpha_3 > 2\alpha_1$, the folded state is shown in Figure 8a, and the radius of the outer circle of the origami pattern is r.

Figure 8b presents a top view of this structure, which shows that the shape's circumscribed circle is formed by a regular hexagon. The fully compacted radius equals the distance between these vertices and the hexagon's centre. The hexagon vertices originate from the farthest points of facet-3 in each unit. As shown in Figure 8b, the maximum circumscribed circle of the shape has its point of displacement at point B. By measuring the displacement of point *B* and its distance to the central axis, denoted as the length *NB*, the folding ratio of this origami pattern can be determined.

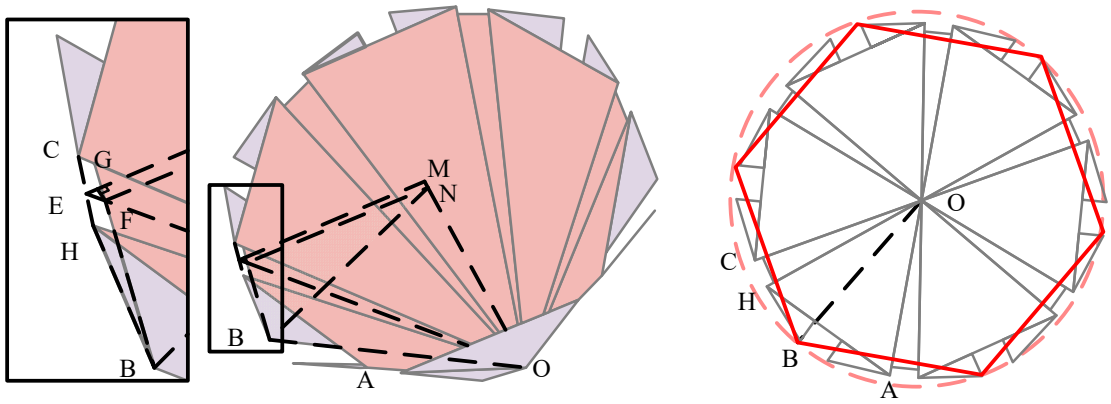

(a) (b)

Figure 8. The Geometric relationships of the folded state when $\alpha_3 > 2\alpha_1$; (**a**) folded configuration; (**b**) the circumscribed circle and inscribed hexagon.

The folding ratio, n, is defined as the ratio of the distance from a vertex on the envelope polygon to the centre of the structure to the radius $l_{OB} = r$. It is calculated as:

$$\begin{aligned} n &= \frac{l_{NB}}{r} = \frac{\sqrt{\left(l_{EM} - l_{EF} \cdot \frac{l_{EM}}{r}\right)^2 + (l_{BF})^2}}{r} \\ &= \sqrt{5{k_1}^2 + 4sin^2\left(\frac{\alpha_2}{2}\right) + 4\sqrt{3}k_1 \sin\left(\frac{\alpha_2}{2}\right)\left(1 - \sqrt{1 - {k_1}^2} + \sqrt{1 - {k_2}^2}\right)^2 + {k_2}^2} \end{aligned} \tag{5}$$

Among

$$k_1 = \sin\left(\frac{\alpha_2 + 2\alpha_3 - \pi/3}{2}\right), k_2 = \sin\left(\frac{\alpha_3}{2}\right)$$

where $\alpha_3 = 2\alpha_1$. The final folding state is shown in Figure 9, and the outer circle radius of the origami pattern is also set to $l_{OB} = r$. Because the ratio of the fan angle between the panels changes, point C, point H, and point E overlap, and the overlap point is denoted by point E.

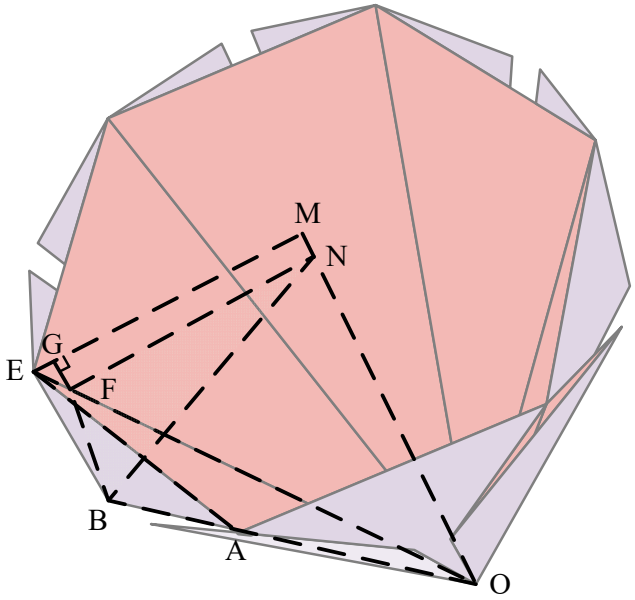

Figure 9. The geometric relationship of the folded state when $\alpha_3 = 2\alpha_1$.

The folding ratio, n, is defined as the ratio of the distance from a vertex on the envelope polygon to the centre of the structure to the radius r. It is calculated as:

$$n = \frac{l_{NB}}{r} = \sqrt{4sin^2\left(\frac{\alpha_2}{2}\right)\cos^2\left(\frac{\alpha_3}{2}\right) + sin^2\left(\frac{\alpha_2}{2}\right)} \tag{6}$$

When $\alpha_3 < 2\alpha_1$, the final folded state is shown in Figure 10. Let the radius of the outer circle of the origami pattern be $l_{OB} = r$, in addition, the long edges of the adjacent facet-2 after folding are coincident, and the short edges points of facet-2 coincide at point E.

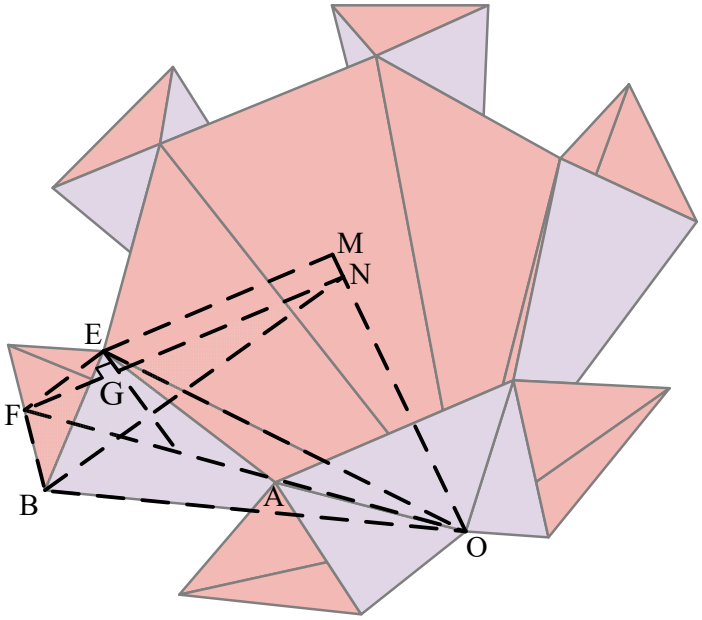

Figure 10. The geometric relationship of the folded state when $\alpha_3 < 2\alpha_1$.

The distance from a vertex on the envelope polygon, formed after folding, to the centre of the structure is

$$\begin{aligned} n &= \frac{l_{NB}}{r} = \frac{\sqrt{l_{NF}^2 + l_{FB}^2}}{r} = \frac{\sqrt{l_{NF}^2 + l_{FB}^2}}{r} \\ &= \frac{\sqrt{(l_{EF}\sin(\angle \mathrm{FEO} - \angle \mathrm{EOM}) + l_{EM})^2 + l_{FB}^2}}{r} \\ &= \sqrt{\left(\sqrt{{k_1}^2 - {k_2}^2}\sin\left[\arccos\left(\frac{4{k_1}^2}{2\sqrt{4{k_1}^2 - {k_2}^2}}\right) - \arcsin\left(2\sin\left(\frac{\alpha_2}{2}\right)\right)\right] + 2\sin\left(\frac{\alpha_2}{2}\right)\right)^2 + {k_2}^2} \end{aligned} \tag{7}$$

Among which,

$$\mathrm{k}_1 = \sin\left(\frac{\alpha_2 + 2\alpha_3 - \pi/3}{2}\right), \mathrm{k}_2 = \sin\left(\frac{\alpha_3}{2}\right)$$

To determine the impact of angle division on the folding ratio of the panels, this paper will follow the calculation and analysis process outlined in Figure 11. First, we designed the initial conditions and input the sector angle ranges for facet-2 and facet-3. For every 0.25° increment, a set of sector angle data will be generated, and the corresponding sector angle for facet1 will be calculated. The program first verifies whether the sector angle data sets and the corresponding sector angle for facet1 are within the acceptable range to ensure that the total sector angles for one unit sum to 60°. Next, it checks for interference by determining if $\angle FBN$ exceeds 60° and if l_{NB} is greater than $2l_{BF}$. The condition $\angle FBN > 60°$ signals that adjacent facets might overlap, while $l_{NB} > 2l_{BF}$ confirms that the overlap is significant. These dual checks help ensure a smooth, interference-free folding process. If any of these

constraints are met, the input data set for the sector angles is marked as invalid and the program moves to the next data set. Otherwise, one of the three predefined calculation methods is selected based on the proportional relationships to calculate the folding ratio. Finally, all valid results are output, and a graph is generated to represent the relationship between the input sector angle data sets and the folding ratio.

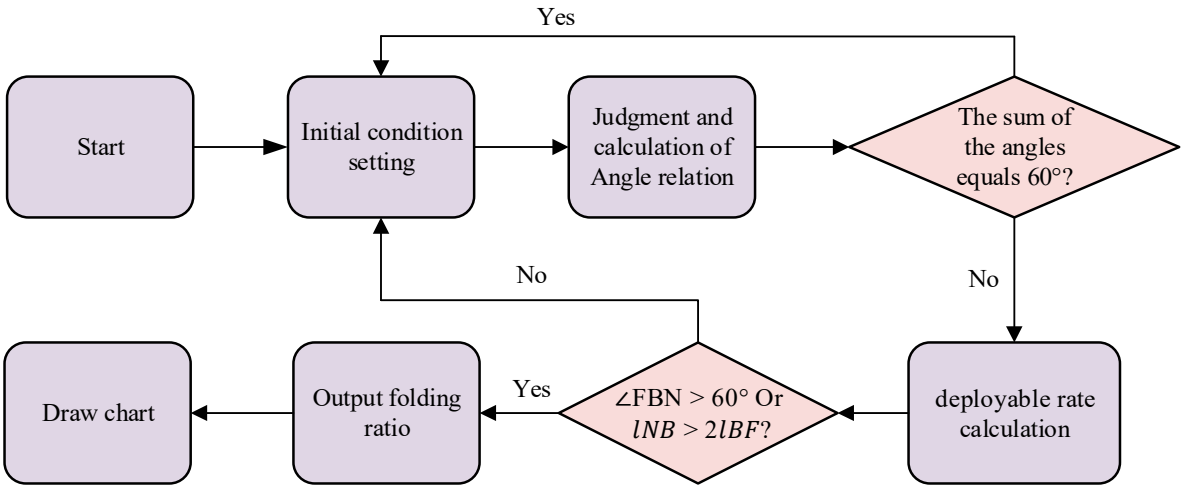

Figure 11. Diagram of the overall parameter calculation process.

Figure 12 illustrates the relationship between facet angles (α_2 on the x-axis, α_3 on the y-axis) and folding ratio, represented by color (blue: low, yellow: high). Under the geometric constraint $2\alpha_1 + \alpha_2 + \alpha_3 = \frac{\pi}{6}$, α_1 is determined once α_2 and α_3 are selected. Two clear trends emerge:

1. Increasing α_2 consistently raises the folding ratio (the colour shifts toward yellow).
2. Increasing α_3 initially increases the ratio but eventually lowers it, forming a low value along the line $\alpha_3 = 2\alpha_1$.

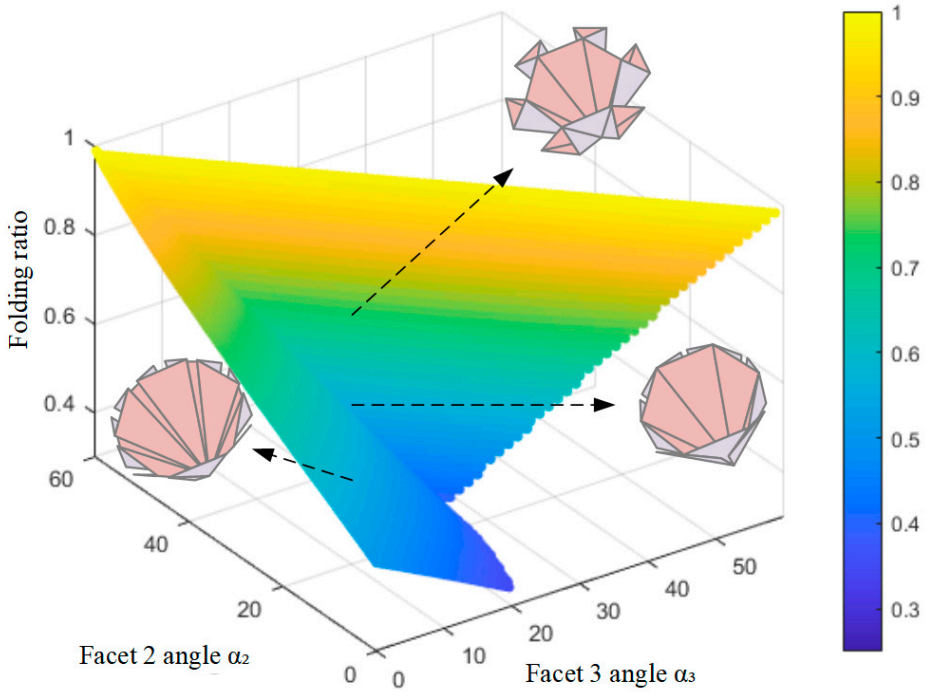

Figure 12. The relationship between facet-2 angle α_2, facet-3 angle α_3, and folding ratio.

The darkest blue region (optimal folding ratio) aligns precisely with $\alpha_3 = 2\alpha_1$, where the ratio reaches its minimum. Designs left of this line ($\alpha_3 > 2\alpha_1$) show higher ratios (blue–green transition), while those to the right ($\alpha_3 < 2\alpha_1$) also underperform (blue–cyan transition). This confirms $\alpha_3 = 2\alpha_1$ as the optimal configuration for the minimizing folding ratio, which we adopted in the thick-panel model to maximize storage efficiency.

3. Mathematical Modelling and Structural Support for Thick-Panel Origami Mechanisms

3.1. Mathematical Model for Thick-Panel Origami Mechanisms

During the transformation of an origami design from a mathematical model to a physical model, converting the origami pattern from a zero-thickness surface to a thick-sheet one is an essential step for engineering applications. In this thickening process, there are two crucial research areas: the impact of thickening on the deployment of the original structure and avoiding potential interference between facets in the thick-sheet origami.

Figure 13 illustrates the transformation from a single-point, multi-crease thick-sheet origami to a ring-shaped single-point, multi-crease thick-sheet origami. This transformation is achieved by dividing the original thick-sheet origami into two parts using a concentric circle with a radius smaller than that of the disk. The inner part becomes a disk, while the outer part becomes a ring-shaped single-point, multi-crease thick-sheet origami. The sector angles of the facets significantly affect the final folding state of the thick-sheet origami and can cause interference between facet-2s in adjacent units. This interference is quantified by the minimum angle between the adjoining edges of two adjacent facet-2s after folding. As the facet thickness increases, this angle becomes larger. When the thickness-to-radius ratio is sufficiently large, the interference angle becomes small enough for the model to approximate a thin-sheet model.

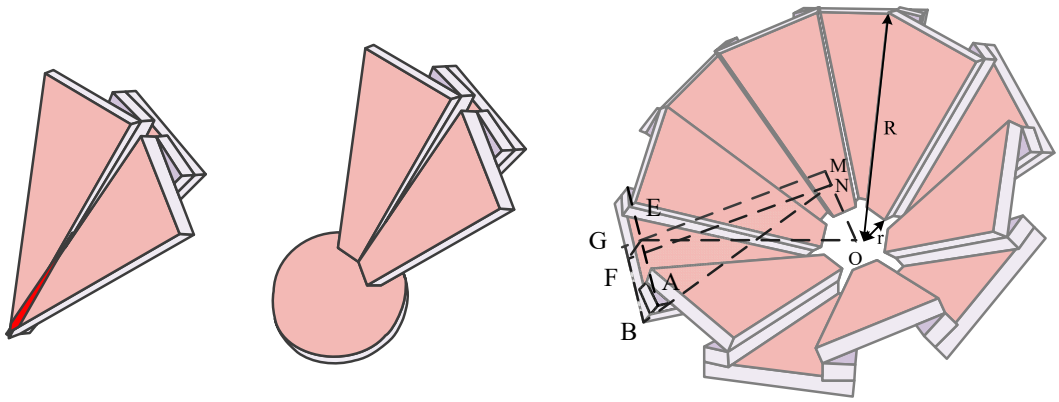

(a) (b) (c)

Figure 13. Comparison of facet interference: (**a**) before modification, with the red area indicating interference; (**b**) after modification, where the interference in the red area is eliminated; (**c**) the array configuration after modification.

For a ring-shaped single-point multi-crease thick-plate model, if the inner diameter is r, the outer diameter is R, the sector angles of facet1, facet-2, and facet-3 are α_1, α_2, and α_3, respectively, and the plate thickness is t, then the folding ratio is:

$$
\begin{aligned}
n &= \frac{l_{NB}}{R} = \frac{\sqrt{{l_{NF}}^2+{l_{FB}}^2}}{R} = \frac{\sqrt{(l_{ME}+l_{EG})^2+{l_{QB}}^2}}{R} \\
&= \frac{1}{R}\left[\begin{array}{l}\left(\cos\left(\alpha_2-\frac{1}{2}\alpha_3\right)(R+r)\cdot\cot\left(\frac{\pi(R+r)}{6(R+r)+\alpha_3 R\sec\left(\alpha_2-\frac{1}{2}\alpha_3\right)}\right)\right. \\ \left.+\frac{2\left(\sqrt{3}+3\right)t(R-\mathrm{r})}{3\left((R-r)^2-\left(\alpha_2 R-\alpha_3 r+2\cos\left(\alpha_2-\frac{1}{2}\alpha_3\right)(R+r)\right)^2\right)^{1/2}}\right)^2 \\ +\frac{(\alpha_2 R)^2}{4}\end{array}\right]^{1/2}
\end{aligned} \tag{8}
$$

3.2. Distribution Methods of Hinges in Thick-Sheet Origami

Dealing with interference between facets is a key issue in the design of thick-sheet origami. Increasing the thickness of the panel can be understood as a translation process. Adjusting the positions of the hinges, which represent the creases, is an effective way to solve this problem. Specifically, there are two stretching methods: one is along the normal directions of each facet, shifting symmetrically to both sides, where the hinges remain aligned in a straight line, as shown in Figure 14a; the other stretches along the normal vector from each facet's reflective surface to its back, changing the hinge distribution, as shown in Figure 14b.

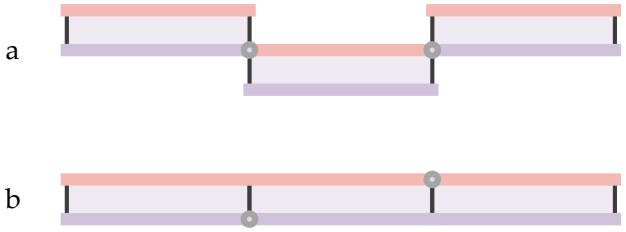

Figure 14. Hinge setup configurations, the red area represents the antenna reflector, while the blue area indicates the back of the panel; (**a**) symmetric translation with linear hinge alignment (circles); (**b**) directional stretching with redistributed hinges (circles).

Among these two methods, the second approach—stretching along the plane's normal vector—is adopted in this design. This movement occurs along the plane's normal vector to accommodate the added thickness. This adjustment ensures the facets avoid overlapping or jamming during movement and maintains proper functionality.

In this design, the hinge positions are distributed along the plane's normal direction, as shown in Figure 14. This method matches the modelling approach used in earlier designs, ensuring consistency in the overall framework. This arrangement minimizes the need for major modifications to the facets. At the same time, the expanded thick-sheet origami achieves a smooth, flat surface after deployment, improving its practicality and usability.

3.3. Design of Rib Support Structure

In order to support the deployment of the SVMCO structure, this section designed a single-degree-of-freedom rib support mechanism.

The rib support mechanism design draws inspiration from the rib structure frilled lizards and proposes a single-degree-of-freedom support system as shown in Figure 15. The rib support mechanism consists of a central support platform, a support frame, and six identical branch link systems. The central support platform includes the central reflective surface (1), lead screw beam (2), and slider (4). The branch link systems are made up of a connecting beam (3), panel connecting hinge (5), and T-shaped beam (6). The fixed support frame (7) provides overall stability to the structure. The structure enables the overall deployment and folding of the system through the upward and downward movement

of the slider (4) along the lead screw beam (2). Each branch link system functions as a parallel mechanism, including a PRR (Prismatic–Revolute–Revolute) branch connected to the central support platform and an R (Revolute) branch connected to the support frame (7). A T-shaped beam (6) connects to the back of the SVMCO panel via a revolute joint.

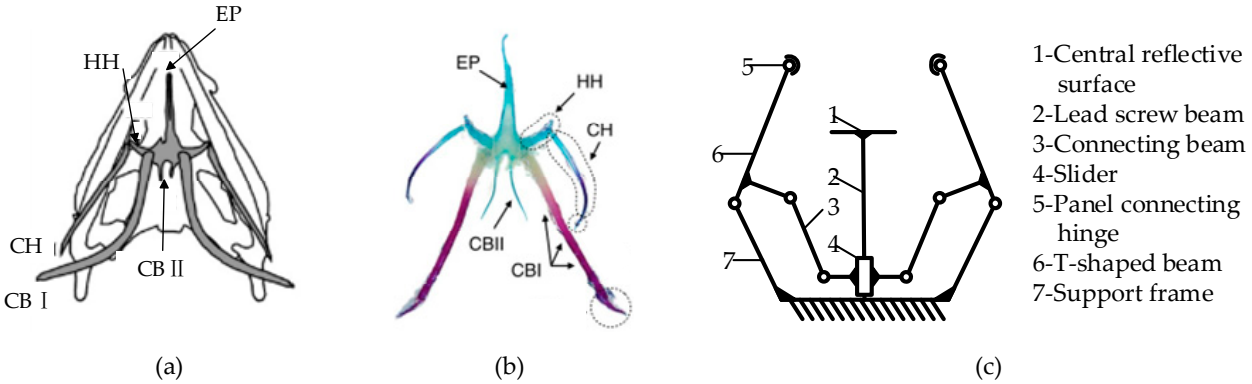

Figure 15. Rib support structure model inspired by the skeletal distribution and connection method of the frilled lizard: (**a**) skeletal structure [46], (**b**) description of the design concept [45], and (**c**) resulting support structure.

In practical applications, the slider (4) along the lead screw beam (2) connected to the central reflective surface (1) of the panel drives the rib support structure. In the folded position, the support structure shown in Figures 16a and 17a. Moving up the slider (4) moves the T-shaped beam (6) and its connection points horizontally outward, deploying the panel. When the panel is fully deployed, the lead screw reaches its maximum travel point and the central platform aligns with the inner circle of the annular panel, as shown in Figures 16b and 17b.

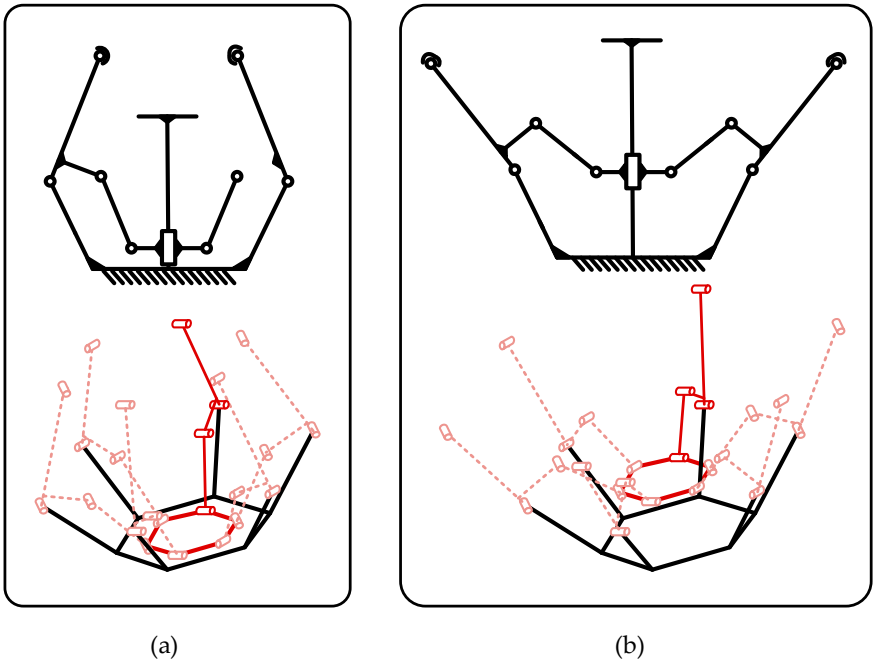

Figure 16. Kinematic sketch of rib support mechanism: (**a**) folded configuration, (**b**) deployable configuration.

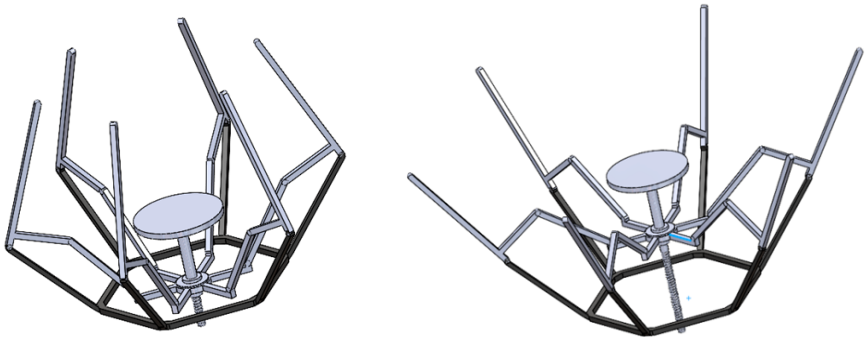

(a) (b)

Figure 17. Rib support structure model: (**a**) folded state, (**b**) deployable state.

This biomimetic design, inspired by the rib mechanism of frilled lizards, improves the deployability and efficiency of the structure, ensuring smooth operation and reducing mechanical interference. The design effectively prevents interference between facets in thick-sheet origami models. Moreover, the design of the back frame ensures control over the degree of freedom of the panel. The folding and deploying of the panel in multiple directions are limited by the single degree of freedom of the back frame, providing stability for the entire mechanism. The motion of the branch links is synchronized, ensuring the uniform deployment of the panel and preventing interference or inconsistent motion, thus ensuring smoothness and precision during the unfolding process.

4. Prototype Design and Analysis

This section will evaluate the prototype developed based on the thickened SVMCO model and compare the theoretical and actual folding ratios as shown in Figure 18. The model was designed with a thickness-to-radius ratio of 3:50. The panel itself is a circular ring with an outer diameter of 1.5 m and an inner diameter of 0.3 m. A physical prototype was then fabricated. The theoretical analysis calculated the folding ratio of the thickened origami pattern model to be 0.51. In contrast, prototype testing showed an actual folding ratio of 0.54, determined through manual measurement of the envelope diameter, which is slightly higher than the predicted value.

The difference between the calculated and actual folding ratios can be attributed to several interconnected factors.

First, manufacturing tolerances may lead to minor deviations in fold angles and facet dimensions, affecting the folding ratio. Additionally, variations in material properties from theoretical assumptions can result in inaccuracies. Furthermore, hinge and joint friction, which are not fully considered in the models, can introduce resistance in the prototype and hinder smooth deployment.

Despite these discrepancies, the close match between the theoretical folding ratio (0.51) and the actual folding ratio (0.54) suggests that the design principles of the thickened origami pattern model are sound.

The result shows that the model effectively creates deployable structures with favourable folding ratios and reduced support requirements, with the prototype tests validating its potential for practical applications.

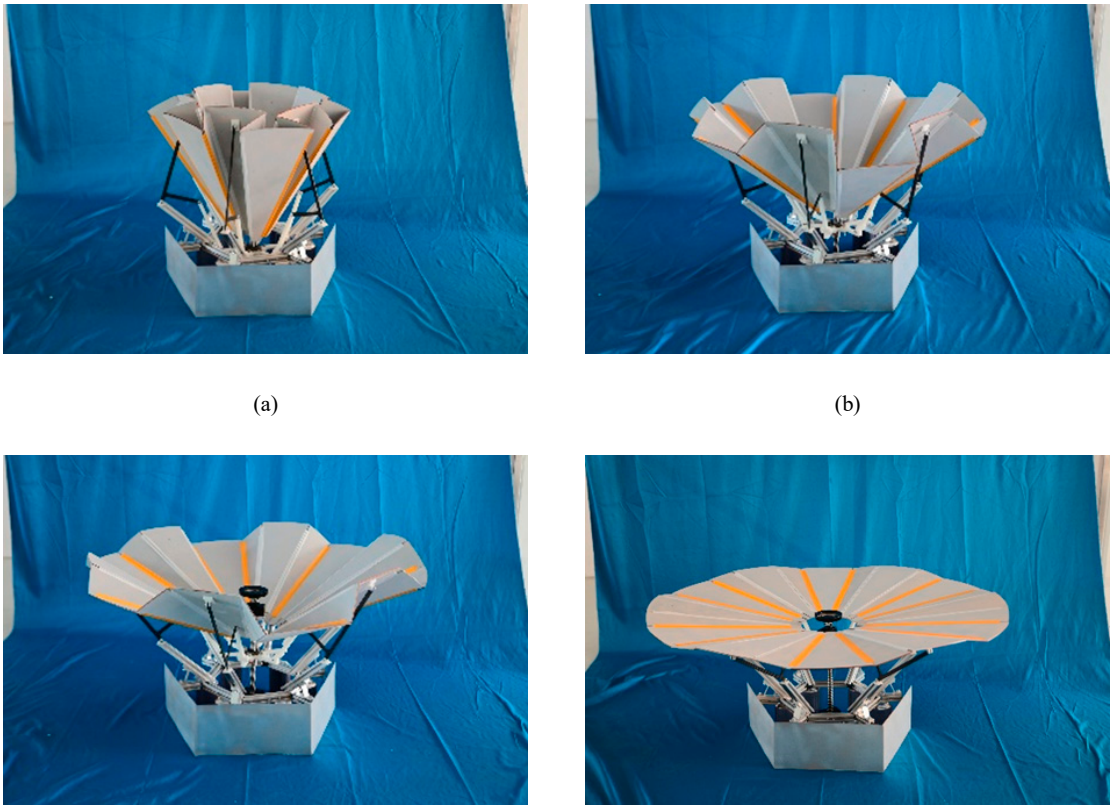

(a) (b)

(c) (d)

Figure 18. Sequence of the prototype's deployment process: (**a**) folded configuration, (**b**) 25% deployed configuration, (**c**) 50% deployed configuration, and (**d**) deployed configuration.

5. Conclusions

This research explored the design and optimization of single-vertex multi-crease origami (SVMCO) patterns, resulting in a deployable structure with improved efficiency.

The analysis examined how the number of units in a single-ring array impacts the folding ratio, revealing that an array with six units achieves the optimal balance between compactness and structural efficiency. A mathematical model linked facet sector angles to folding performance, identifying that the optimal folding ratio occurs when the minimum facet sector angle is half the maximum.

This model also accounted for panel thickness, inner diameter, and outer diameter to determine the best design for given parameters. Inspired by bionic principles, the study introduced a rib support system mimicking natural structures, enhancing stability and usability. A prototype with a 1.5 m radius validated this design, showcasing a theoretical folding ratio of 0.51 and an actual folding ratio of 0.54.

The structure demonstrated high deployability, reduced support requirements, and a smooth reflective surface. These findings contribute to deployable structures with practical applications and inspire further research into bionic-inspired designs and advanced engineering implementations.

Future work will focus on extending this planar structure to curved surfaces, which is critical for applications such as deployable antennas. Key challenges include the design of specialised hinges to accommodate curvature and the development of thick-plate origami techniques to address material thickness limitations. Advancing work in these areas will improve the structural integrity and functionality of deployable systems in aerospace and communications applications.

Author Contributions: Conceptualization, Y.W. and B.H.; methodology, Y.W.; investigation, Y.W., B.H., M.H. and J.D.; writing—original draft preparation, Y.W.; writing—review and editing, Y.Z., B.H., M.H. and J.Y.; validation, J.D.; formal analysis, J.D.; supervision, Y.Z., B.H. and J.Y.; funding acquisition, Y.Z. and B.H. All authors have read and agreed to the published version of the manuscript.

Funding: This work was supported by the National Natural Science Foundation of China [Nos. 52105035 and 62203094], the Special Central Funds for Guiding Local Scientific and Technological Development [No. 236Z1801G], the Higher Education Youth Top Talent Project of Hebei Province of China [No. BJK2024042], the Natural Science Foundation of Hebei Province of China [Nos. E2021203109 and F2023501021] and the Graduate Student Innovation Capability Training and Support Project of Hebei Province [No. CXZZBS2024053].

Data Availability Statement: Data are contained within the article.

Conflicts of Interest: The authors declare no conflicts of interest.

Abbreviations

The following abbreviations are used in this manuscript:

AHP	Analytic Hierarchy Process
SVMCO	single-vertex multi-crease origami

References

1. Ma, X.; Li, T.; Ma, J.; Wang, Z.; Shi, C.; Zheng, S.; Cui, Q.; Li, X.; Liu, F.; Guo, H.; et al. Recent Advances in Space-Deployable Structures in China. *Engineering* **2022**, *17*, 207–219. [CrossRef]
2. Han, B.; Xu, Y.; Yao, J.; Zheng, D.; Li, Y.; Zhao, Y. Design and analysis of a scissors double-ring truss deployable mechanism for space antennas. *Aerosp. Sci. Technol.* **2019**, *93*, 105357. [CrossRef]
3. Han, B.; Yuan, Z.; Hu, X.; Xu, Y.; Yao, J.; Zhao, Y. Design and analysis of a hoop truss deployable antenna mechanism based on convex pentagon polyhedron unit. *Mech. Mach. Theory* **2023**, *186*, 105365. [CrossRef]
4. Kim, T.-H.; Suh, J.-E.; Han, J.-H. Deployable truss structure with flat-form storability using scissor-like elements. *Mech. Mach. Theory* **2021**, *159*, 104252. [CrossRef]
5. Han, B.; Zhang, J.C.; Liu, F.; Han, M.; Xu, Y.D.; Yao, J.T. Structural design and surface networking analysis of a truss antenna based on hexagonal frustum deployable mechanism units. *Thin-Walled Struct.* **2024**, *202*, 112160. [CrossRef]
6. Han, B.; Yuan, Z.T.; Hu, X.Y.; Zhang, J.C.; Xu, Y.D.; Yao, J.T. Kinematic Characteristics Analysis and Assembly Application of the Rectangular Pyramid Deployable Mechanism. *AIAA J.* **2024**, *62*, 1775–1788. [CrossRef]
7. Han, B.; Zhou, Y.; Zhang, J.; Xu, Y.; Yao, J.; Zhao, Y. Kinematics and dynamics characteristics analysis of a double-ring truss deployable mechanism based on rectangular scissors unit. *Eng. Struct.* **2024**, *307*, 117900. [CrossRef]
8. Ji, J.C.; Luo, Q.; Ye, K. Vibration control based metamaterials and origami structures: A state-of-the-art review. *Mech. Syst. Signal Process.* **2021**, *161*, 107945. [CrossRef]
9. Vlachaki, E.; Liapi, K.A. Hybrid origami-linkage vaulted deployable structures: Parametric development and form-finding. *Meccanica* **2024**. [CrossRef]
10. Tang, Y.Y.; Liu, J.G.; Wu, C.C.; Zhao, P.Y. Configuration design and crease topology of origami-inspired spinning space deployable structures. *Proc. Inst. Mech. Eng. Part C-J. Mech. Eng. Sci.* **2024**, *238*, 5621–5637. [CrossRef]
11. Zhang, J.; Zhang, L.; Wang, C. Kresling origami-inspired reconfigurable antenna with spherical cap. *Int. J. Mech. Sci.* **2022**, *227*, 107470. [CrossRef]
12. Fonseca, L.M.; Rodrigues, G.V.; Savi, M.A. An overview of the mechanical description of origami-inspired systems and structures. *Int. J. Mech. Sci.* **2022**, *223*, 107316. [CrossRef]
13. Suh, J.E.; Miyazawa, Y.; Yang, J.Y.; Han, J.H. Self-Reconfiguring and Stiffening Origami Tube. *Adv. Eng. Mater.* **2022**, *24*, 2101202. [CrossRef]
14. Han, B.; Yuan, Z.; Zhang, J.; Xu, Y.; Yao, J.; Zhao, Y. Design and analysis of modular deployable antenna mechanism based on a class of self-limiting position units. *Mech. Mach. Theory* **2024**, *191*, 105509. [CrossRef]
15. Li, Y.; Pan, F.; Lin, X.; Yang, K.; Ren, Y.; Yang, W.; Chen, Y. Multistable origami honeycomb. *Int. J. Mech. Sci.* **2023**, *243*, 108044. [CrossRef]
16. Wang, H.; He, Y.; Yu, A.; Li, X.; Gu, M.; Ling, X.; Chen, G. Origami-inspired structures with programmable multi-step deformation. *Mech. Adv. Mater. Struct.* **2022**, *31*, 1182–1197. [CrossRef]

17. Shen, W.; Jiang, X.; Zhang, Z.; Okudan-Kremer, G.E.; Qin, H. An origami-inspired infill pattern for additive manufacturing to reinforce the energy absorption performance. *Int. J. Adv. Manuf. Technol.* **2022**, *122*, 4267–4274. [CrossRef]
18. Pavon, R.M.; Bazan, A.M.; Cepa, J.J.; Alvarez, A.A.A.; Trigueros, J.M.A.; Alberti, M.G.; Tellaeche, J.R. New Use of BIM-Origami-Based Techniques for Energy Optimisation of Buildings. *Appl. Sci. Basel* **2022**, *12*, 1496. [CrossRef]
19. Shah, S.I.H.; Bashir, S.; Ashfaq, M.; Altaf, A.; Rmili, H. Lightweight and Low-Cost Deployable Origami Antennas—A Review. *IEEE Access* **2021**, *9*, 86429–86448. [CrossRef]
20. Cretella, V.; Sohouli, A.; Pagani, A.; Suleman, A. Linear and nonlinear topology optimization of origami structures based on crease pattern and axial rigidity. *Struct. Multidiscip. Optim.* **2024**, *67*, 78. [CrossRef]
21. Fan, Z.; Wang, R.; Huang, H.; Li, X. Design and Analysis of an Origami-inspired Modular Thick-panel Deployable Structure. *Int. J. Mech. Sci.* **2024**, *282*, 109579. [CrossRef]
22. Ebrahimi Fakhari, H.; Rosario Barboza, J.; Mardanpour, P. Biomimetic Origami: A Biological Influence in Design. *Biomimetics* **2024**, *9*, 600. [CrossRef] [PubMed]
23. Du, C.; Zhao, D. Design and Rapid Prototyping of Deformable Rotors for Amphibious Navigation in Water and Air. *Machines* **2024**, *12*, 837. [CrossRef]
24. Saito, K.; Pérez-de la Fuente, R.; Arimoto, K.; Seong, Y.a.; Aonuma, H.; Niiyama, R.; You, Z. Earwig fan designing: Biomimetic and evolutionary biology applications. *Proc. Natl. Acad. Sci. USA* **2020**, *117*, 17622–17626. [CrossRef]
25. Morgan, J. *An Approach for Designing Origami-Adapted Products with Aerospace Mechanism Examples*; Brigham Young University: Provo, UT, USA, 2015.
26. Fei, L.; Sujan, D. Origami Theory and Its Applications: A Literature Review. *Int. J. Humanit. Soc. Sci.* **2013**, *7*, 229–233.
27. Wang, C.; Guo, H.; Liu, R.; Deng, Z. A programmable origami-inspired space deployable structure with curved surfaces. *Eng. Struct.* **2022**, *256*, 113934. [CrossRef]
28. Xing, D.V.; You, Z. Kinematic behaviour of origami combining two four-crease vertices. *Mech. Res. Commun.* **2023**, *134*, 104213. [CrossRef]
29. Liu, W.R.; Bai, X.; Yang, H.; Bao, R.X.; Liu, J.Q. Tendon Driven Bistable Origami Flexible Gripper for High-Speed Adaptive Grasping. *Ieee Robot. Autom. Lett.* **2024**, *9*, 5417–5424. [CrossRef]
30. Jiang, H. EML webinar overview: Origami-based metamaterials. *Extrem. Mech. Lett.* **2022**, *50*, 101543. [CrossRef]
31. Wang, H.; Qu, H.; Wang, X.; He, Y.; Guo, S. Tensile behavior of square-twist origami inspired mechanical metamaterials with soft joints and chirality applications. *Smart Mater. Struct.* **2024**, *33*, 065038. [CrossRef]
32. Filipov, E.T.; Liu, K.; Tachi, T.; Schenk, M.; Paulino, G.H. Bar and hinge models for scalable analysis of origami. *Int. J. Solids Struct.* **2017**, *124*, 26–45. [CrossRef]
33. Eidini, M.; Paulino, G.H. Unraveling metamaterial properties in zigzag-base folded sheets. *Sci. Adv.* **2015**, *1*, e1500224. [CrossRef] [PubMed]
34. Feng, Y.J.; Huang, X.R.; Qiu, X.M. Bistable morphology analysis of the flexible single-vertex origami unit cell. *Extrem. Mech. Lett.* **2023**, *65*, 102101. [CrossRef]
35. Panina, G.; Streinu, I. Flattening Single-vertex Origami: The Non-expansive Case. In Proceedings of 25th Annual Symposium on Computational Geometry, Aarhus Univ, Aarhus, Denmark, 8–10 June 2009; pp. 306–313.
36. Chen, Y.; Lu, C.H.; Yan, J.Y.; Feng, J.; Sareh, P. Intelligent computational design of scalene-faceted flat-foldable tessellations. *J. Comput. Des. Eng.* **2022**, *9*, 1765–1774. [CrossRef]
37. Wang, W.; Qiu, X. Coupling of Creases and Shells. *J. Appl. Mech.* **2017**, *85*, 011009. [CrossRef]
38. Zhu, Y.; Filipov, E.T. A bar and hinge model for simulating bistability in origami structures with compliant creases. *J. Mech. Robot.* **2020**, *12*, 021110. [CrossRef]
39. Bentley, C.S.; Harne, R.L. Acoustic Wave Focusing From Reconfigurable Acoustic Arrays Based on a Bricard-Miura Synthesis. *J. Vib. Acoust.-Trans. Asme* **2022**, *144*, 041014. [CrossRef]
40. Lv, W.L.; Chen, Y.; Zhang, J.J. Thick-Panel Origami Tubes With Hexagonal Cross-Sections. *J. Mech. Robot. Trans. Asme* **2023**, *15*, 051012. [CrossRef]
41. Chen, Y.; Fan, L.; Bai, Y.; Feng, J.; Sareh, P. Assigning mountain-valley fold lines of flat-foldable origami patterns based on graph theory and mixed-integer linear programming. *Comput. Struct.* **2020**, *239*, 106328. [CrossRef]
42. Zhang, Q.; Qiu, H.; Lin, Q.; Feng, J.; Cai, J. Uniform stretching behavior of single crease origami arrays. *Int. J. Solids Struct.* **2024**, *302*, 112993. [CrossRef]
43. Yang, F.F.; Zhang, M.; Ma, J.Y.; You, Z.; Yu, Y.; Chen, Y.; Paulino, G.H. Design of Single Degree-of-Freedom Triangular Resch Patterns with Thick-panel Origami. *Mech. Mach. Theory* **2022**, *169*, 104650. [CrossRef]
44. Zhao, C.; Li, M.; Zhou, X.; Liu, T.; Xing, J.; Chen, Y.; Zhang, X. Deployable structure based on double-layer Miura-ori pattern. *Mech. Res. Commun.* **2023**, *131*, 104152. [CrossRef]

45. Montandon, S.A.; Fofonjka, A.; Milinkovitch, M.C. Elastic instability during branchial ectoderm development causes folding of the Chlamydosaurus erectile frill. *eLife* **2019**, *8*, e44455. [CrossRef]
46. Ord, T.J.; Klomp, D.A.; Garcia-Porta, J.; Hagman, M. Repeated evolution of exaggerated dewlaps and other throat morphology in lizards. *J. Evol. Biol.* **2015**, *28*, 1948–1964. [CrossRef] [PubMed]

Disclaimer/Publisher's Note: The statements, opinions and data contained in all publications are solely those of the individual author(s) and contributor(s) and not of MDPI and/or the editor(s). MDPI and/or the editor(s) disclaim responsibility for any injury to people or property resulting from any ideas, methods, instructions or products referred to in the content.